Heterodyne-detected stimulated photon echo: applications to optical dynamics in solution

de Boeij, W.P.; Pshenichnikov, M.S; Wiersma, D. A.

Published in:
Chemical Physics

DOI:
10.1016/S0301-0104(98)00084-6

Publication date:
1998

ELSEVIER

Chemical Physics 233 (1998) 287–309

Chemical Physics

Heterodyne-detected stimulated photon echo: applications to optical dynamics in solution

Wim P. de Boeij, Maxim S. Pshenichnikov, Douwe A. Wiersma *

Department of Chemistry, Materials Science Centre, University of Groningen, Nijenborgh 4, 9747 AG Groningen, The Netherlands

Received 1 December 1997

Abstract

Heterodyne detection of the stimulated photon echo (HSPE) is discussed and applied to explore molecular solvation dynamics. With this technique the in-phase and in-quadrature parts of the induced transient nonlinear polarization can be time-gated. A third-order perturbative description of the HSPE is presented, which shows that the transient polarization provides direct information on the real and imaginary components of the nonlinear optical response functions of the system. In the spectral diffusion limit and for impulsive excitation conditions, analytical expressions for the HSPE signal are derived and model calculations are presented. This novel technique is applied to a nonlinear optical study of the dye molecule DTTCI dissolved in ethylene glycol. Several effects are analyzed in detail as, for instance, the intriguing interference effect between the conventional and virtual echo contributions to the total HSPE signal. Furthermore, it is shown that from HSPE measurements the instantaneous frequency of the emitted (nonlinear polarization induced) signal can be derived and that its time-dependent shift projects directly onto the dynamical Stokes shift and the energy reorganization process of the coupled solute–solvent complex. It will also be shown that the experimental data can be simulated using the multimode Brownian oscillator model.

1. Introduction

Recent achievements in femtosecond laser technology [1] and developments in the generation and control of ultrashort laser pulses [2–5] are having an immense impact on time-domain coherent nonlinear spectroscopy [6–10]. Nowadays, numerous nonlinear optical coherence experiments are routinely used to explore various transient features in all fields of science [9,10]. This technological development has also quickly advanced our insight and understanding of solvation dynamics, a process at the focus of our grasp of chemical reactivity [11–15].

From an experimental viewpoint, the study of solvation dynamics by means of optical methods relies on the ability to accurately monitor the induced optical nonlinear polarization. Knowledge of both the amplitude and

* Corresponding author. Present address: Ultrafast Laser and Spectroscopy Laboratory, Materials Science Centre, University of Groningen, Nijenborgh 4, 9747 AG Groningen, The Netherlands. E-mail: d.a.wiersma@chem.rug.nl

[1] For an overview on recent advances in femtosecond laser technology, see Ref. [1].

0301-0104/98/$19.00
PII: S0301-0104(98)00084-6

the phase of the nonlinear signal is indispensable for the reconstruction of the complex nonlinear response function that describes the interaction between the optical radiation and the system under investigation.

If the nonlinear optical polarization is induced by a sequence of well-defined pulses, one of the excitation pulses can simply be used to project the induced nonlinear polarization onto its in-phase and in-quadrature parts. The method we are referring to is the heterodyne method of detection which is based on an optical interference between the signal field and the local oscillator field. In this paper we apply the technique of phase-locked excitation [16–18] towards the heterodyne detection of the stimulated photon echo [19], as proposed by Cho et al. [20]. Phase-locked excitation provides the opportunity to control the phase between the local oscillator and the emitted nonlinear signal. In this way the in-phase and in-quadrature components of the induced nonlinear polarization can be measured, which provides full information on the nonlinear response function of the system.

In this paper, the heterodyne detection method of the stimulated photon echo will be used towards the study of solvation dynamics. We will focus on the transient real and imaginary parts of the nonlinear polarization and explore the dependence on the excitation conditions (e.g., timing of the incident pulses). In previous studies, the time-integrated as well as the time-gated stimulated photon echo technique have been applied towards the study of the optical dynamics in liquids [21–43]. Based on results from these type of measurements, the Bloch model [44], conventionally used for the description of optical dynamics in condensed phase systems, was proven to be insufficient [21]. Stochastic modulation models [45,46] allowed for a better description of the systems dynamics, be it that the dynamical fluorescence Stokes shift, a distinct property of dissolved chromophores, was not predicted in this model [29]. Note that the dynamical Stokes shift is a direct indication of the presence of an energy relaxation process involving both the solute and solvent. Lately much attention has been addressed towards the understanding of this particular energy reorganizational process, since they are of extreme importance in the electron transfer systems [47–51], and (primary) biological functional units [52–55].

The inadequacy of the stochastic model in the description of energy relaxation processes, stimulated the development of more advanced models. By modelling of the system–bath interaction by means of a set of intermediating harmonic oscillators, each coupled to a distribution of harmonic bath modes, the spin–boson Hamiltonian and multimode Brownian oscillator model (MBO) was developed [47,56–68]. In this paper the MBO model will be applied to describe the HSPE data.

The organization of the paper is as follows: in Section 2 the theoretical analysis of the heterodyne-detected stimulated photon echo (HSPE) is presented. In Section 3 we perform numerical simulations based on a model system to highlight different aspects of the HSPE. Section 4 deals with the details of experimental set-up. Results of HSPE experiments as well as numerical simulations based on the multimode Brownian oscillator (MBO) model are discussed in Section 5. Section 6 concludes the paper.

2. Theoretical background

In this section the heterodyne detection of the stimulated photon echo is presented. A third-order perturbative description of the induced nonlinear polarization (echo signal) and the heterodyne detection of the induced stimulated photon echo are addressed.

2.1. Heterodyne detection of nonlinear polarization

A perturbative description of the interaction of optical radiation with matter is well established [68–70]. In this formalism, the polarization induced by excitation pulses is decomposed in the terms ordered in powers of the electric field:

$$\begin{aligned} P^{\mathrm{tot}} &= P^{(1)} + P^{(3)} + P^{(5)} + \ldots \\ &\propto \mathrm{i}\, R^{(1)}E + \mathrm{i}^3 R^{(3)}EEE + \mathrm{i}^5 R^{(5)}EEEEE + \ldots \end{aligned} \quad . \tag{1}$$

The appearance of only the odd terms in the series results from the macroscopic isotropy of the medium, leading to a cancellation of the even terms. Although in a formal treatment the response functions as given in Eq. (1) are represented by tensors and the electric fields as well as the polarizations by vectors, we restrict ourselves here to a scalar approach.

In this treatment we will only consider the third-order nonlinear polarization although incorporation of any higher-order approximation is straightforward [66]. The pulse sequence of the stimulated photon echo is depicted in Fig. 1. Three short optical pulses E_1, E_2 and E_3 induce a nonlinear optical polarization P^{tot} which in turn serves as a source of the signal field [71]:

$$E_{\mathrm{S}}(t) = \frac{\mathrm{i}\omega}{2\epsilon_0 c} P^{\mathrm{tot}}(t)\, l \sin c(\Delta k l/2) \exp(\mathrm{i}\Delta k l/2)\,, \tag{2}$$

where l is the length of the sample, c the speed of light, and Δk the phase-mismatch factor. Eq. (2) was derived in the limit of media with low optical density and assuming that the electric fields are plane waves with slowly varying envelopes. Recently it was shown that Eq. (2) holds well even for the pulses containing a single oscillation at the optical frequency [72]. Under the conditions of perfect phase matching, $\Delta k = 0$, the sinc length dependence as well as the additional phase factor are eliminated, and the induced polarization $P^{\mathrm{tot}}(t)$ is directly proportional (but $\pi/2$ phase-shifted!) to the emitted electric signal field $E_{\mathrm{S}}(t)$. In the HSPE experiment, the phase-matching conditions are satisfied automatically due to the choice of the wavevectors of the interacting fields (Fig. 1). Furthermore, the fourth field $E_4(t)$ having the same wavevector as the signal field ($\boldsymbol{k}_2$) serves as a local oscillator $E_{\mathrm{LO}}(t)$ in a heterodyne detection scheme. The observed quantity is the interference term between the local oscillator field E_{LO} and the signal field (induced polarization):

$$S_{\mathrm{HSPE}}(t_{34}, t_{23}, t_{12}) \propto \mathrm{Im} \int_0^\infty \mathrm{d}t P^{(3)}(t, t_{23}, t_{12}) \times E^*_{\mathrm{LO}}(t - t_{34})\,. \tag{3}$$

Contrary to the homodyne detection method that probes the modulus square of the induced polarization induced signal, in the heterodyne detection scheme the signal is linearly proportional to the induced polarization. Furthermore, by controlling the phase relation between the signal field and the local oscillator, the in-phase and in-quadrature projections of the nonlinear polarization can be directly measured. Knowledge of these two projections is sufficient to fully characterize the nonlinear induced signal.

We would like to discuss briefly the approximations made upon deriving Eq. (3). First of all, we disregard the homodyne term proportional to $|P^{(3)}|^2$. This is reasonable since the electric field induced due to a nonlinear interaction is usually much weaker than a local oscillator field derived right from the laser. However, one should be aware of the fact that in some circumstances this approximation may not be warranted [73,74]. Second, we assume that the third-order polarization dominates the total nonlinear response. Therefore, in order to minimize the interference of the third- with fifth- and higher-order polarizations (like $P^{(3)}P^{(5)*}$), low-intensity pulses

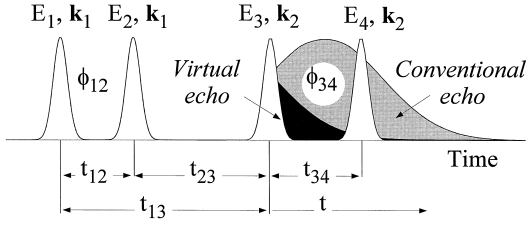

Fig. 1. Pulse sequence in the heterodyne detection of the photon echo experiment. The relevant delays between the excitation pulses (t_{12}, t_{23}, t_{34}, t_{13}, t) are indicated in the figure. The wavevectors of the excitation pulses are given adjacent the electric fields. The local oscillator field is depicted as the fourth pulse (E_4). The relative phases between the first–second pulses and the third–fourth pulses are denoted by ϕ_{12} and ϕ_{34}, respectively. An artist impression of the conventional echo (gray) and virtual echo (black) are presented after the third pulse.

should be applied to the sample. Since the ratio between the fifth- and third-order polarizations scales proportionally to the intensity of the applied fields ($P^{(5)}/P^{(3)} \propto I$), a lower intensity relatively enhances the third-order polarization. Third, free-induction decay (FID) induced by the third excitation pulse as well as the local oscillator field, can subsequently act as a second local oscillator in the HSPE experiment. This effect can elongate the effective temporal and phase resolution of the experiment. Fortunately, the FID amplitude is proportional to the sample concentration while the amplitude of the third-order response scales with the square of the concentration. Therefore, the influence of the FID can be disregarded in the limit of a low optical density. All these limitations should be recalled when an HSPE experiment is made.

2.2. Heterodyne detection of the stimulated photon echo

A description of the generation of the nonlinear polarization relies on a third-order perturbative expansion of the density matrix evolution. For a detailed overview on the response function theory, density matrix evolution in the Liouville phase space, we refer the reader to the monograph of Mukamel [68]. Based on this formalism, the following expression for the third-order nonlinear polarization generated in a two-level system, emerges:

$$P^{(3)}(t, t_{23}, t_{12}) \propto N\left(\frac{\mathrm{i}}{\hbar}\right)^3 \int_0^\infty \mathrm{d}t_3 \int_0^\infty \mathrm{d}t_2 \int_0^\infty \mathrm{d}t_1 \left[R_{\mathrm{A}}(t_3, t_2, t_1) + R_{\mathrm{B}}(t_3, t_2, t_1) \right], \tag{4}$$

where N is the sample concentration. The response functions R_{A} and R_{B} are respectively given by:

$$\begin{aligned} R_{\mathrm{A}}(t_3, t_2, t_1) = {} & \left[R_{\mathrm{II}}(t_3, t_2, t_1) + R_{\mathrm{III}}(t_3, t_2, t_1) \right] \times E_3(t - t_{23} - t_{12} - t_3)\, E_2(t - t_{12} - t_3 - t_2) \\ & \times E_1^*(t - t_3 - t_2 - t_1) \exp\left[-\mathrm{i}(\omega_{\mathrm{eg}} - \omega)(t_3 - t_1) \right], \end{aligned} \tag{5a}$$

$$\begin{aligned} R_{\mathrm{B}}(t_3, t_2, t_1) = {} & \left[R_{\mathrm{I}}(t_3, t_2, t_1) + R_{\mathrm{IV}}(t_3, t_2, t_1) \right] \times E_3(t - t_{23} - t_{12} - t_3)\, E_2^*(t - t_{12} - t_3 - t_2) \\ & \times E_1(t - t_3 - t_2 - t_1) \exp\left[-\mathrm{i}(\omega_{\mathrm{eg}} - \omega)(t_3 + t_1) \right]. \end{aligned} \tag{5b}$$

In Eqs. (5), $R_{\mathrm{I}}(t_3, t_2, t_1)$ to $R_{\mathrm{IV}}(t_3, t_2, t_1)$ denote the third-order nonlinear response functions for the corresponding double-sided Feynman diagrams (Fig. 2). The diagrams represent the time-domain evolution of the density matrix upon the sequential interaction with the optical fields and free evolution during the time in between the interactions [68].

For the diagrams R_{II} and R_{III}, the evolution of the density matrix exhibits an inversion: the coherent superposition state $|g\rangle\langle e|$ during time t_1 is inverted $|e\rangle\langle g|$ during time t_3. In the system that is at least partly inhomogeneously broadened, the signal arising from these two pathways is delayed with respect to the last excitation pulse and usually denoted as the photon echo. In case of the presence of a overwhelming inhomogeneity, the echo signal peaks at the classical (Bloch–Hahn) time: $t = t_{12}$ [69]. For the diagrams R_{I} and R_{IV} the inversion of the coherence during times t_1 and t_2 does not occur. Therefore, these diagrams are usually denoted as non-rephasing contributions and have historically been assigned to the so-called virtual echo [75–77]. In case of an inhomogeneously broadened system the virtual echo would have peaked at negative times ($t < 0$); however, as a result of causality, only the tail of the virtual echo contribution is observed in experiment. Furthermore note that the diagrams R_{I} and R_{II} describe the evolution through an excited population state ($|e\rangle\langle e|$) during the waiting time t_{23} while for the diagrams R_{III} and R_{IV} the system evolves through a ground state $|g\rangle\langle g|$. We will later show that a separation based on the ground- or excited-state character of the evolution is experimentally impossible since the contributions from the ground and excited states are strongly intertwined.

For a full insight in the optical dynamics of the system both the real as well as the imaginary parts of the nonlinear response functions should be determined. To achieve this goal, heterodyne detection methods can be applied, where the detected signal is linearly proportional to the induced nonlinear polarization and directly relates to the desired nonlinear response functions (Eq. (3)). Since in the heterodyne detection experiment the

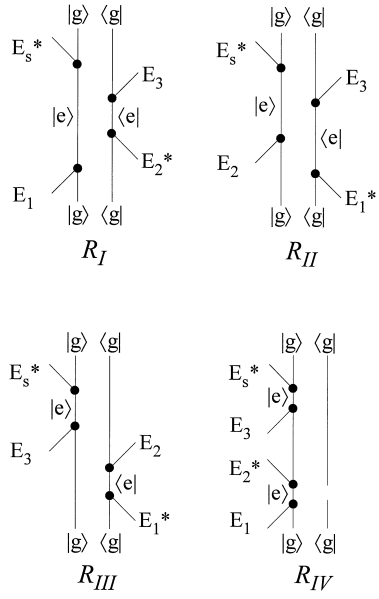

Fig. 2. The four relevant double-sided Feynman diagrams describing the evolution of the reduced density matrix elements as applicable to the HSPE experiment. The different pathways corresponding to the particular response functions, are denoted by R_{I}, R_{II}, R_{III}, R_{IV}. The vertices indicate interactions with the electric fields, while the electric fields are given next to the vertices. $|g\rangle\langle g|$and $|e\rangle\langle e|$ denote the ground- and excited-state reduced density matrix elements, respectively. The off-diagonal coherences are given by $|e\rangle\langle g|$ and $|g\rangle\langle e|$.

signal field is interferometrically mixed with the local oscillator field, the relative phase between the two interacting optical fields must be properly defined and stabilized. The actual phase of the final HSPE signal depends on the individual phases of the three incident laser pulses, therefore the necessary phase condition involves all phase settings of the applied pulses. Taking into consideration the phase-matching geometry as used in the HSPE experiment, two phase differences should be defined: the relative phase (ϕ_{12}) between the first pulse pair (E_1–E_2), and the relative phase (ϕ_{34}) for the second pulse pair (E_3–E_4).

Nowadays sophisticated methods exist for the controlled shaping of femtosecond laser pulses [78–80]. However, given the complexity of these methods as well as the required investments, we apply here the technique of phase-locked pulses as introduced by Scherer et al. [16–18]. The latter method utilizes an interferometer for the preparation of the phase-related optical pulse pair. Unlike cw-laser interferometers where the relative phase between the optical fields can directly be determined from the interference signal intensity, non-time-overlapping pulse do not produce such an interference pattern in space. However, when these time-separate pulses are monitored after a narrowband monochromator, a spectral interferogram can be observed. The frequency-domain expression for the spectral interferogram (I_{tot}) is given by:

$$I_{\mathrm{tot}}(\omega-\omega_{\mathrm{lock}}) = 2\,I_{\mathrm{s}}(\omega-\omega_{\mathrm{lock}}) \times \left(1+\cos\left[(\omega-\omega_{\mathrm{lock}})\tau+\phi\right]\right), \tag{6}$$

where I_{s} is the single pulse spectrum, ω_{lock} a fixed monochromator setting, ω the detuning from the fixed value, τ the delay and ϕ the relative phase between the laser pulses. The shape of the interferogram (i.e., the intensity at the monochromator setting ω_{lock}) strongly changes as the delay and relative phase between the pulses is changed. As an example, we present in Fig. 3 the interferograms for the in-phase and the in-quadrature phase setting. Based on the particular intensity at the so-called lock frequency ω_{lock}, the phase relation between the time-separated laser pulses can be set and maintained during the data acquisition time. From Eq. (6) it follows that the relative phase delay between two pulses is related to the lock frequency and the actual delay between the pulses, t_{12} as:

$$\phi_{12}^{\mathrm{total}} = \phi_1 - \phi_2 = (\omega-\omega_{\mathrm{lock}})\,t_{12} + \phi_{12}\,, \tag{7}$$

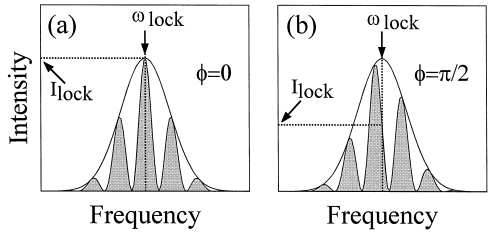

Fig. 3. Intensity spectrum (spectral interferogram) of a double-pulse sequence in a phase-locked configuration. In the left panel, the relative phase between the pulses is set to $\phi = 0$ while in the right panel $\phi = \pi/2$. The position of the lock frequency is indicated by the arrow. The spectral intensity at the lock frequency (I_{lock}) changes for different phase settings. The single pulse spectrum (multiplied by 4) is given by the dashed line for comparison.

where ω is the laser carrier frequency. From the experimental point of view, the lock wavelength is the wavelength for which the automatic feedback control system adjusts the phase to a value ϕ_{12}. Mismatch between the laser carrier frequency and the lock frequency results in an additional component in the phase directly related to the actual delay t_{12}. Of course, a similar relation holds for the phase-delay between the third and fourth (local oscillator) pulse:

$$\phi_{34}^{\mathrm{total}} = \phi_3 - \phi_4 = (\omega - \omega_{\mathrm{lock}})t_{34} + \phi_{34}\,. \tag{8}$$

For chirp-free excitation pulses (i.e., the pulses which temporal phase is constant) we can recast Eqs. (5) as:

$$\begin{aligned} R_{\mathrm{A}}(t_3,t_2,t_1) = {} & \left[R_{\mathrm{II}}(t_3,t_2,t_1) + R_{\mathrm{III}}(t_3,t_2,t_1)\right] \\ & \times A_3(t - t_{23} - t_{12} - t_3)\,A_2(t - t_{12} - t_3 - t_2)\,A_1(t - t_3 - t_2 - t_1) \\ & \times \exp\left[-\mathrm{i}(\omega_{\mathrm{eg}} - \omega)(t_3 - t_1) + \mathrm{i}(\omega - \omega_{\mathrm{lock}})(t_{12} - t_{34}) - \mathrm{i}\phi_{12} + \mathrm{i}\phi_{34}\right], \end{aligned} \tag{9a}$$

$$\begin{aligned} R_{\mathrm{B}}(t_3,t_2,t_1) = {} & \left[R_{\mathrm{I}}(t_3,t_2,t_1) + R_{\mathrm{IV}}(t_3,t_2,t_1)\right] \\ & \times A_3(t - t_{23} - t_{12} - t_3)\,A_2^{*}(t - t_{12} - t_3 - t_2)\,A_1(t - t_3 - t_2 - t_1) \\ & \times \exp\left[-\mathrm{i}(\omega_{\mathrm{eg}} - \omega)(t_3 + t_1) - \mathrm{i}(\omega - \omega_{\mathrm{lock}})(t_{12} + t_{34}) + \mathrm{i}\phi_{12} + \mathrm{i}\phi_{34}\right], \end{aligned} \tag{9b}$$

where A_i denotes the transient amplitude of the ith pulse. Eqs. (9) together with Eqs. (3) and (4) is the key result in the theoretical description of HSPE. They allow to calculate the HSPE signal for any given electric fields and response functions depending on specifics in the system–bath interaction. These equations generalize the earlier description of HSPE [20], where the system was a priori assumed to be overwhelmingly inhomogeneously broadened. Consequently, the pathways I and IV were neglected and the echo signal was supposed to peak at the classical time $t = t_{12}$. We will see below that these assumptions are not justified at all for real molecular systems.

2.3. Impulsive approximation

In the impulsive limit, i.e. when the duration of all four pulses are considerably shorter than the inverse bandwidth of the transition, the integrals in the equations for the polarization (Eqs. (3) and (4)) can be evaluated, and the expression for the HSPE signal reads:

$$\begin{aligned} S_{\mathrm{HSPE}}(t_{34},t_{23},t_{12}) \propto {} & \mathrm{Re}\Big\{\left[R_{\mathrm{II}}(t_{34},t_{23},t_{12}) + R_{\mathrm{III}}(t_{34},t_{23},t_{12})\right] \\ & \times \exp\left[-\mathrm{i}(\omega_{\mathrm{eg}} - \omega_{\mathrm{lock}})(t_{34} - t_{12}) - \mathrm{i}\phi_{12} + \mathrm{i}\phi_{34}\right] \\ & + \left[R_{\mathrm{I}}(t_{34},t_{23},t_{12}) + R_{\mathrm{IV}}(t_{34},t_{23},t_{12})\right] \\ & \times \exp\left[-\mathrm{i}(\omega_{\mathrm{eg}} - \omega_{\mathrm{lock}})(t_{34} + t_{12}) + \mathrm{i}\phi_{12} + \mathrm{i}\phi_{34}\right]\Big\}. \end{aligned} \tag{10}$$

Furthermore, selection of the lock wavelength equal to the transition wavelength ($\omega_{\mathrm{lock}} = \omega_{\mathrm{eg}}$), results in:

$$\begin{aligned} S_{\mathrm{HSPE}}(t_{34}, t_{23}, t_{12}) \propto\ & \mathrm{Re}\{R_{\mathrm{II}}(t_{34}, t_{23}, t_{12}) + R_{\mathrm{III}}(t_{34}, t_{23}, t_{12})\}\cos[\phi_{12} - \phi_{34}] \\ & + \mathrm{Im}\{R_{\mathrm{II}}(t_{34}, t_{23}, t_{12}) + R_{\mathrm{III}}(t_{34}, t_{23}, t_{12})\}\sin[\phi_{12} - \phi_{34}] \\ & + \mathrm{Re}\{R_{\mathrm{I}}(t_{34}, t_{23}, t_{12}) + R_{\mathrm{IV}}(t_{34}, t_{23}, t_{12})\}\cos[\phi_{12} + \phi_{34}] \\ & - \mathrm{Im}\{R_{\mathrm{I}}(t_{34}, t_{23}, t_{12}) + R_{\mathrm{IV}}(t_{34}, t_{23}, t_{12})\}\sin[\phi_{12} + \phi_{34}]. \end{aligned} \tag{11}$$

The above expression represents the most general case for the phase settings ϕ_{12} and ϕ_{34}. We consider here four combinations of the in-phase ($\phi = 0$) and in-quadrature ($\phi = \pi/2$) settings of the phases:

$$S_{\mathrm{HSPE}}(\phi_{12} = 0, \phi_{34} = 0) = \mathrm{Re}\{R^{\mathrm{echo}} + R^{\mathrm{virt.echo}}\}, \tag{12a}$$

$$S_{\mathrm{HSPE}}(\phi_{12} = \pi/2, \phi_{34} = 0) = \mathrm{Im}\{R^{\mathrm{echo}} - R^{\mathrm{virt.echo}}\}, \tag{12b}$$

$$S_{\mathrm{HSPE}}(\phi_{12} = 0, \phi_{34} = \pi/2) = -\mathrm{Im}\{R^{\mathrm{echo}} + R^{\mathrm{virt.echo}}\}, \tag{12c}$$

$$S_{\mathrm{HSPE}}(\phi_{12} = \pi/2, \phi_{34} = \pi/2) = \mathrm{Re}\{R^{\mathrm{echo}} - R^{\mathrm{virt.echo}}\}, \tag{12d}$$

where

$$R^{\mathrm{echo}} = R_{\mathrm{II}} + R_{\mathrm{III}}, \tag{13a}$$

$$R^{\mathrm{virt.echo}} = R_{\mathrm{I}} + R_{\mathrm{IV}}. \tag{13b}$$

Measurement of the 'orthogonal' HSPE signals as given by Eqs. (12) allows for a full reconstruction of the real and imaginary part of both the rephasing (R^{echo}) and non-rephasing ($R^{\mathrm{virt.echo}}$) part of the response function. Note that whatever experimental phase combination is selected, a full separation in contributions from the ground state (R_{III} and R_{IV}) and the excited state (R_{I} and R_{II}) is not possible, since both signals are always grouped together in the expressions.

Depending on the specific selection of phase ϕ_{12}, the contributions from the conventional echo and the virtual echo can be made to interfere constructively or destructively. Constructive interference occurs whenever the relative phase between the first and second pulses is set to $\phi_{12} = 0$. Destructive interference occurs for the in-quadrature condition, $\phi_{12} = \pi/2$. Control over this interference mechanism can be exercised since the relative phase within the pulse pairs can be set to any value. Inspection of Eqs. (12) furthermore shows that the question whether the real or imaginary part of the response function is probed depends on both the phases. Is the total sum ($\phi_{12} + \phi_{34}$) equal to 0 or π, the real part of the response function is the observable quantity. A total phase ($\phi_{12} + \phi_{34}$) equal to $\pi/2$ results in the detection of the imaginary part of the response function.

By inversion of Eqs. (12) the complex response functions can be expressed in terms of HSPE signals:

$$R^{\mathrm{echo}} + R^{\mathrm{virt.echo}} \propto S_{\mathrm{HSPE}}(\phi_{12} = 0, \phi_{34} = 0) - \mathrm{i}S_{\mathrm{HSPE}}(\phi_{12} = 0, \phi_{34} = \pi/2), \tag{14a}$$

$$R^{\mathrm{echo}} - R^{\mathrm{virt.echo}} \propto S_{\mathrm{HSPE}}(\phi_{12} = \pi/2, \phi_{34} = \pi/2) + \mathrm{i}S_{\mathrm{HSPE}}(\phi_{12} = \pi/2, \phi_{34} = 0). \tag{14b}$$

Since the complete complex character of the nonlinear response functions is known, we can now retrieve the amplitude (A) and phase (Φ) that is defined as follows.

$$R^{\mathrm{echo}} \pm R^{\mathrm{virt.echo}} = A^{\mathrm{echo} \pm \mathrm{virt.echo}} \times \exp^{\mathrm{i}\Phi^{\mathrm{echo} \pm \mathrm{virt.echo}}}. \tag{15}$$

The time-dependent amplitude is easily obtained by taking the modulus of Eqs. (14) and reads:

$$A^{\mathrm{echo+virt.echo}}(t_{34}, t_{23}, t_{12}) \propto |S_{\mathrm{HSPE}}(\phi_{12} = 0, \phi_{34} = 0) - \mathrm{i}S_{\mathrm{HSPE}}(\phi_{12} = 0, \phi_{34} = \pi/2)|, \tag{16a}$$

$$A^{\mathrm{echo-virt.echo}}(t_{34}, t_{23}, t_{12}) \propto |S_{\mathrm{HSPE}}(\phi_{12} = \pi/2, \phi_{34} = \pi/2) + \mathrm{i}S_{\mathrm{HSPE}}(\phi_{12} = \pi/2, \phi_{34} = 0)|. \tag{16b}$$

Also the time-dependent phase (Φ) of the response functions can be extracted and reads:

$$\Phi^{\text{echo}+\text{virt.echo}}(t_{34}, t_{23}, t_{12}) \propto \arctan\left(\frac{-S_{\text{HSPE}}(\phi_{12}=0, \phi_{34}=\pi/2)}{S_{\text{HSPE}}(\phi_{12}=0, \phi_{34}=0)} \right) \tag{17}$$

for the constructive interference case and

$$\Phi^{\text{echo}+\text{virt.echo}}(t_{34}, t_{23}, t_{12}) \propto \arctan\left(\frac{S_{\text{HSPE}}(\phi_{12}=\pi/2, \phi_{34}=0)}{S_{\text{HSPE}}(\phi_{12}=\pi/2, \phi_{34}=\pi/2)} \right) \tag{18}$$

for the destructive interference situation. Once the phase is determined, the time derivative of the phase directly gives the instantaneous frequency of the emitted signal:

$$\omega_{\text{inst}}(t_{34}, t_{23}, t_{12}) = \frac{\partial \Phi(t_{34}, t_{23}, t_{12})}{\partial t_{34}} . \tag{19}$$

Changes in the instantaneous frequency ω_{inst} as the excitation conditions (i.e., the delay t_{23}) provide crucial insight in the possible energy relaxation pathways and relaxation kinetics. In fact, Eq. (19) directly reflects the dynamical Stokes shift.

3. Numerical calculations

We now discuss a particular example of the system–bath interaction: the so-called spectral diffusion limit. Under this approximation, the system can be regarded as inhomogeneously broadened on the time scale of t_{12} and t_{34} (but not t_{23}). Although this limit is not directly applicable to a description of optical dynamics in liquids, the spectral diffusion model allows to derive readily analytical expressions for the HSPE signal. Furthermore, the typical signal shapes, sensitivity to the system–bath dynamics and interference effects provide altogether good insight in the basic features of the HSPE technique.

3.1. Spectral diffusion approximation

The third-order response functions $R_{\text{I}}, \ldots, R_{\text{IV}}$ can be derived making use of a cumulant expansion, which gives [68]:

$$R_{\text{I}}(t_3, t_2, t_1) = \exp\left[-g^*(t_3) - g(t_1) - g^*(t_2) + g^*(t_2+t_3) + g(t_1+t_2) - g(t_1+t_2+t_3) \right] , \tag{20a}$$

$$R_{\text{II}}(t_3, t_2, t_1) = \exp\left[-g^*(t_3) - g^*(t_1) + g(t_2) - g(t_2+t_3) - g^*(t_1+t_2) + g^*(t_1+t_2+t_3) \right] , \tag{20b}$$

$$R_{\text{III}}(t_3, t_2, t_1) = \exp\left[-g(t_3) - g^*(t_1) + g^*(t_2) - g^*(t_2+t_3) - g^*(t_1+t_2) + g^*(t_1+t_2+t_3) \right] , \tag{20c}$$

$$R_{\text{IV}}(t_3, t_2, t_1) = \exp\left[-g(t_3) - g(t_1) - g(t_2) + g(t_2+t_3) + g^*(t_1+t_2) - g(t_1+t_2+t_3) \right] . \tag{20d}$$

The key function in the above equations is the so-called line broadening function $g(t)$, which is related to the oscillator–bath correlation function $M(t)$ in the following way (chap. 8 of Ref. [68]):

$$g(t) = \Delta^2 \int_0^t \mathrm{d}\tau_1 \int_0^{\tau_1} \mathrm{d}\tau_2 \, M(\tau_2) - \mathrm{i}\lambda \int_0^t \mathrm{d}\tau \left[1 - M(\tau) \right] . \tag{21}$$

For the sake of simplicity, we have assumed that the high-temperature limit applies in Eq. (21). A more general

case is analysed elsewhere [68]. Analytical expressions for the correlation functions $M(t)$ can be derived, for instance, in the Brownian oscillator model [68].

In this section we restrict ourselves to a simple case, namely the spectral diffusion limit, where the correlation function does not change appreciably at the time scale t_{12} and t_{34} (but not t_{23}). Performing a Taylor expansion around the time t_{23}, the following set of expressions for the behaviour of the real and imaginary part, respectively, of the lineshape function can be derived:

$$g_{\mathrm{Re}}(t_{23}+t) = g_{\mathrm{Re}}(t_{23}) + \Delta^2 t \int_0^{t_{23}} M(\tau)\mathrm{d}\tau + \tfrac{1}{2}\Delta^2 t^2 M(t_{23}), \tag{22a}$$

$$g_{\mathrm{Im}}(t_{23}+t) = g_{\mathrm{Im}}(t_{23}) - \lambda t\big[1 - M(t_{23})\big]. \tag{22b}$$

From Eqs. (22), one finds the following relations for the short-time behaviour of the line-shape function:

$$g_{\mathrm{Re}}(t\to 0) = \tfrac{1}{2}\Delta^2 t^2, \tag{23a}$$

$$g_{\mathrm{Im}}(t\to 0) = 0. \tag{23b}$$

Upon substitution Eqs. (22) and (23) into Eqs. (20), the following relations are found from Eqs. (13):

$$R^{\mathrm{echo}}(t_{34},t_{23},t_{12}) = \exp\!\big(-\tfrac{1}{2}\Delta^2 t_{12}^2 - \tfrac{1}{2}\Delta^2 t_{34}^2 + \Delta^2 t_{12} t_{34} M(t_{23})\big) \times \big\{1 + \exp\!\big(2\mathrm{i}\lambda t_{34}\big[1 - M(t_{23})\big]\big)\big\}, \tag{24a}$$

$$R^{\mathrm{virt.echo}}(t_{34},t_{23},t_{12}) = \exp\!\big(-\tfrac{1}{2}\Delta^2 t_{12}^2 - \tfrac{1}{2}\Delta^2 t_{34}^2 - \Delta^2 t_{12} t_{34} M(t_{23})\big) \times \big\{1 + \exp\!\big(2\mathrm{i}\lambda t_{34}\big[1 - M(t_{23})\big]\big)\big\}. \tag{24b}$$

Inspection of the real part of the above response functions shows a difference in the sign of the cross term (proportional to $t_{12}t$). This is a direct manifestation of the rephasing (positive sign in R^{echo}) or non-rephasing character (negative sign in $R^{\mathrm{virt.echo}}$) of the corresponding Liouville pathways. The term that is associated with the rephasing contributions yields a delayed signal transient (Fig. 1) which peaks at the time $t = M(t_{23})^* t_{12}$ (photon echo). The signal related to the second, nonrephasing contribution $R^{\mathrm{virt.echo}}$, is usually referred to as *virtual echo*. Mathematically, the virtual echo would have rephased at negative times, but because of causality only the tail of the virtual echo is observed as depicted schematically in Fig. 1.

The resulting expressions for the total HSPE signal are given by:

$$\begin{aligned} S^{(3)}_{\mathrm{tot}}(t_{34},t_{23},t_{12}) \;\propto\; & A^{\mathrm{echo}}(t_{34},t_{23},t_{12}) \times \Big[\cos^2\!\big\{\lambda t_{34}\big(M(1-t_{23})\big)\big\} \times \cos(\phi_{12}-\phi_{34}) \\ & + \tfrac{1}{2}\sin\!\big\{2\lambda t_{34}\big(1 - M(t_{23})\big)\big\} \times \sin(\phi_{12}-\phi_{34})\Big] \\ & + A^{\mathrm{virt.echo}}(t_{34},t_{23},t_{12}) \times \Big[\cos^2\!\big\{\lambda t_{34}\big(M(1-t_{23})\big)\big\} \times \cos(\phi_{12}+\phi_{34}) \\ & - \tfrac{1}{2}\sin\!\big\{2\lambda t_{34}\big(1 - M(t_{23})\big)\big\} \times \sin(\phi_{12}+\phi_{34})\Big], \end{aligned} \tag{25}$$

where the amplitude functions A^{echo} and $A^{\mathrm{virt.echo}}$ are given by:

$$A^{\mathrm{echo}}(t_{34},t_{23},t_{12}) = \exp\!\big(-\tfrac{1}{2}\Delta^2 t_{12}^2\big[1 - M^2(t_{23})\big]\big) \times \exp\!\Big(-\tfrac{1}{2}\Delta^2\big[t_{34} - M(t_{23})t_{12}\big]^2\Big), \tag{26a}$$

$$A^{\mathrm{virt.echo}}(t_{34},t_{23},t_{12}) = \exp\!\big(-\tfrac{1}{2}\Delta^2 t_{12}^2\big[1 - M^2(t_{23})\big]\big) \times \exp\!\Big(-\tfrac{1}{2}\Delta^2\big[t_{34} + M(t_{23})t_{12}\big]^2\Big) \tag{26}$$

Now, when both the real and imaginary parts of the total HSPE signal are known, we can retrieve the instantaneous frequency of the signal (confer Eqs. (17) and (19)):

$$\omega_{\mathrm{inst}}(t_{23}) = \frac{\partial \Phi(t_{23},t_{24})}{\partial t_{34}} = \frac{\partial}{\partial t_{34}}\left[\arctan\left(\frac{-S^{(3)}_{\mathrm{tot}}(\phi_{12}=0,\phi_{34}=\pi/2)}{S^{(3)}_{\mathrm{tot}}(\phi_{12}=0,\phi_{34}=0)}\right)\right] = \lambda\big[M(t_{23}) - 1\big]. \tag{27}$$

From the above equation it follows that the instantaneous frequency shift of the signal is directly connected to

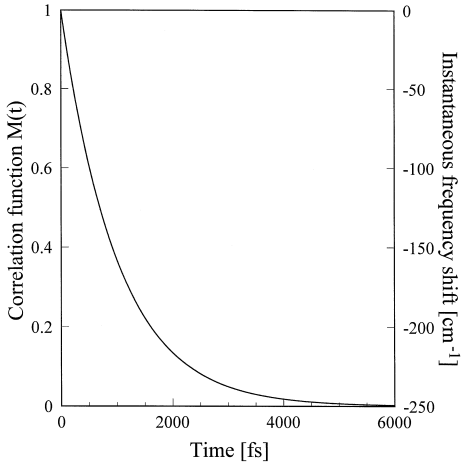

Fig. 4. The correlation function $M(t)$ as used in the model calculations. The right-hand axis marks the instantaneous frequency shift at the different settings of the delay t_{23}.

the value of the correlation function at the time t_{23}. For short times t_{23} ($M(t_{23}) \approx 1$), Eq. (27) gives a shift equal to zero, whereas the long-term shift ($M(t_{23}) \approx 0$) approaches $-\lambda$. This value is in fact the average between the total Stokes shift in the excited state of -2λ and the static ground state (no shift). Note that the emergence of a time-dependent instantaneous signal frequency, is a direct manifestation of an imaginary part in the system response functions.

3.2. Model calculations

In this section we calculate the HSPE signals for a model system that consists of two electronic levels coupled to the bath by means of a single strongly overdamped Brownian oscillator. The correlation function for such a system is given by [68]:

$$M(t) = \exp(-\Lambda t)\,. \tag{28}$$

In our simulations, the coupling parameter of the oscillator amounts to $\Delta = 60$ THz, whereas the inverse correlation time is $\Lambda = 1$ THz (Fig. 4). With the correlation time of $\tau_c = 1/\Lambda = 1$ ps, the restrictions set in the previous paragraph, are fully met. The slow correlation time of the oscillator furthermore puts the calculation in the high-temperature limit, where a direct relation exists between the coupling strength Δ and the reorganizational energy parameter λ [68]:

$$\lambda = \Delta^2\hbar/(2k_B T_k)\,. \tag{29}$$

The results of the numerical calculations for the HSPE signals are presented in Fig. 5 for the four orthogonal HSPE signals. The signals are calculated as a function of t_{34} that is the delay between the last excitation pulse and the local oscillator pulse, for different delays between the second and the third pulse (t_{23}).

The most striking feature of the signals depicted in Fig. 5 is the appearance of signals for negative times t_{34}. Given the causality of the third-order response, the signal can only emerge after it has interacted with the third pulse. However, due to the specific phase-matching arrangement (Fig. 1), the HSPE signals for negative times results from the fact that upon scanning the delay t_{34} from positive values to negative values, the third and the fourth pulses are interchanged. It is this effect in combination with the selection of the phase difference between the last interaction pulse (third pulse) and the local oscillator pulse (fourth pulse), that determines whether a symmetric signal or an antisymmetric signal is measured along the t_{34} coordinate. For an in-phase setting of the relative phase ϕ_{34} ($\phi_{34} = 0$), the pulses are fully indistinguishable upon exchange. For the in-quadrature

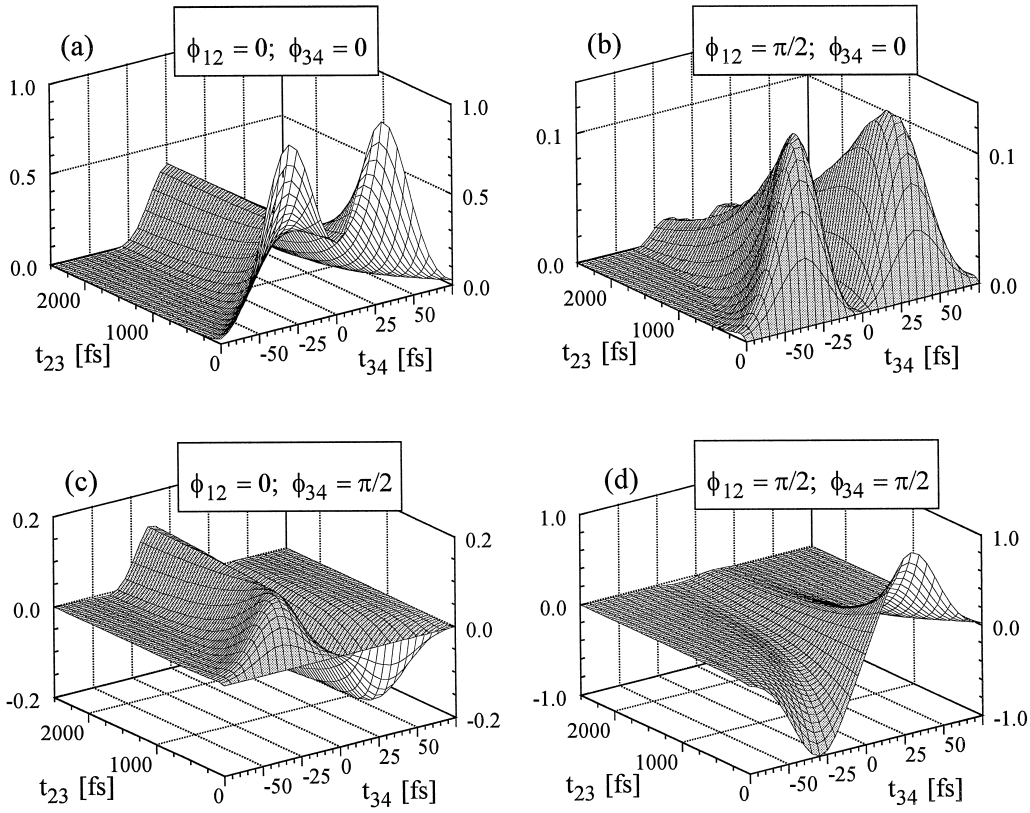

Fig. 5. Numerical calculations for the heterodyne detected photon echo signals measured under four orthogonal phase settings: (a) $\phi_{12} = 0$; $\phi_{34} = 0$; (b) $\phi_{12} = \pi/2$, $\phi_{34} = 0$; (c) $\phi_{12} = 0$, $\phi_{34} = \pi/2$; and (d) $\phi_{12} = \pi/2$, $\phi_{34} = \pi/2$. The system coupling parameter is $\Delta = 60$ THz. The correlation function is given by: $M(t) = \exp(-\Lambda t)$, where $\Lambda = 1$ THz (Fig. 4). The delay between the pulses 1 and 2 is set to $t_{12} = 30$ fs.

condition ($\phi_{34} = \pi/2$), the phase is changed from $+\pi/2$ to $-\pi/2$ upon changing the t_{34}-delay from positive to negative values which results in an antisymmetric signal along the t_{34} coordinate.

Let us first focus on Fig. 5a, where the signal for the phase conditions $\phi_{12} = 0$ and $\phi_{34} = 0$, is depicted:

$$S^{(3)}(t_{34}, t_{23}, t_{12}) = \cos^2\left(\lambda t_{34}\left[1 - M(t_{23})\right]\right) \times \left\{A^{\text{echo}}(t_{34}, t_{23}, t_{12}) + A^{\text{virt.echo}}(t_{34}, t_{23}, t_{12})\right\}. \quad (30)$$

In the above expression the contributions from the conventional echo and the virtual echo are positioned symmetric around time $t_{34} = 0$ and peak at times $t_{34} = \pm M(t_{23}) * t_{12}$. Note that the position of the maximum of this function scales proportional to the actual value of the correlation function at time t_{23}, $M(t_{23})$ and the initial setting of the delay t_{12}. The modulation term presented by the cosine term, only slightly affects the signal shape. In fact, this term is constant and equal 1 for $M(t_{23}) = 1$ and causes only a slightly narrowing of the signal for $M(t_{23}) = 0$. The inherent coupling between the value of the energy reorganization term λ and the coupling strength Δ (Eq. (29)) results in a relatively small additional modulation of the cosine term in the final signal.

For delay time t_{23} close to zero ($M(t_{23}) \approx 1$), a delayed transient signal (Fig. 5a) indicates the presence of significant inhomogeneous contribution. For short times t_{23}, the correlation function has not yet decayed significantly, the phase memory is still preserved, and a rephasing of the system evolution is thus possible. A delayed echo response is formed (Fig. 5a), which peaks at a time $t_{34} \approx t_{12}$:

$$S^{(3)}(t_{34}, t_{23}, t_{12}) = \left\{\exp\left(-\tfrac{1}{2}\Delta^2\left[t_{34} - t_{12}\right]^2\right) + \exp\left(-\tfrac{1}{2}\Delta^2\left[t_{34} + t_{12}\right]^2\right)\right\}. \quad (31)$$

Only the tail of the virtual echo (the second term in Eq. (31)) is seen for positive times.

As the waiting time t_{23} increases, a narrowing of the signal and a decrease in the signal amplitude is observed (Fig. 5a). For long times t_{23}, a t_{23}-delay-independent signal is seen. This situation corresponds to the case where the correlation function has nearly decayed to zero. The conventional echo and virtual echo are now indistinguishable. In this limit the expression for the signal is given by:

$$S^{(3)}_{t_{23}\to\infty}(t_{34}, t_{23}, t_{12}, \phi_{12}=0, \phi_{34}=0) = 2\cos^2(\lambda t_{34}) \times \exp\left(-\tfrac{1}{2}\Delta^2 t_{12}^2\right) \times \exp\left(-\tfrac{1}{2}\Delta^2 t_{34}^2\right). \quad (32)$$

Destructive interference between the conventional and virtual echoes occurs if the phase settings $\phi_{12}=\pi/2$ and $\phi_{34}=\pi/2$ are taken. The signal expression for this situation is:

$$S^{(3)}(t_{34}, t_{23}, t_{12}) = \cos^2\left(\lambda t_{34}\left[1-M(t_{23})\right]\right) \times \left\{A^{\text{echo}}(t_{34}, t_{23}, t_{12}) - A^{\text{virt.echo}}(t_{34}, t_{23}, t_{12})\right\}. \quad (33)$$

In Eq. (33) the destructive interference between the terms is evident from the presence of a minus sign in between the conventional and virtual echoes (compare to Eq. (30)). The calculated HSPE signals for this case are depicted in Fig. 5d. As a result of the in-quadrature phase setting of the phase $\phi_{34}=\pi/2$, an antisymmetric signal is found, with nearly the same amplitude as for the in-phase conditions ($\phi_{12}=0$, $\phi_{34}=0$). As the time t_{23} increases ($M(t_{23})\to 0$), the virtual and conventional echo merge together and eventually have identical shapes (consult Eqs. (26)). Destructive interference between these two echo contributions leads to a full cancellation of the signal. Note that the disappearance of the signal is based on destructive interference between two contributions and not on the fact that each contribution vanishes separately. The last statement can be easily checked by examining Fig. 5a, demonstrating the presence of a signal at large times t_{23}.

Similar constructive and destructive interference effects can be observed in case the imaginary part of the response function is probed ($\phi_{12}=0$, $\phi_{34}=\pi/2$ or $\phi_{12}=\pi/2$, $\phi_{34}=0$). The corresponding signal expressions for these conditions are:

$$S^{(3)}(t_{34}, t_{23}, t_{12}) = -\tfrac{1}{2}\sin\left(2\lambda t_{34}\left[1-M(t_{23})\right]\right) \times \left\{A^{\text{echo}}(t_{34}, t_{23}, t_{12}) + A^{\text{virt.echo}}(t_{34}, t_{23}, t_{12})\right\} \quad (34)$$

and

$$S^{(3)}(t_{34}, t_{23}, t_{12}) = \tfrac{1}{2}\sin\left(2\lambda t_{34}\left[1-M(t_{23})\right]\right) \times \left\{A^{\text{echo}}(t_{34}, t_{23}, t_{12}) - A^{\text{virt.echo}}(t_{34}, t_{23}, t_{12})\right\}, \quad (35)$$

respectively.

The first equation presents the constructive interference, whereas the latter relation presents the destructive interference between the conventional and virtual echo. The calculated signals are depicted in Fig. 5c and b, respectively. Inspection of Eqs. (34) and (35) again reveals the two (Gaussian) contributions for echo and virtual echo signals. Similar as was described for the signals in Fig. 5a and d, the signals measured under cross-phase conditions ($\phi_{12}=0$, $\phi_{34}=\pi/2$ and $\phi_{12}=\pi/2$, $\phi_{34}=0$) exhibits similar interference phenomena. Fig. 5c presents the case for the constructive interference whereas in Fig. 5b the destructive interference situation holds. For large delay times t_{23}, the signal depicted in Fig. 5b decays as a result of the fact that the virtual and conventional echoes merge in time, leading to perfect destructive interference. The appearance of the constructive or the destructive interference between the different contributions is fully determined by the setting of the phase ϕ_{12}. Constructive interference between the two contributions (conventional and virtual echo) occurs for $\phi_{12}=0$, destructive interference for a phase setting $\phi_{12}=\pi/2$. Whether the real or imaginary part of the induced polarization and thus the response function is measured, depends on both the phase setting ϕ_{12} and ϕ_{34}. If the sum of the phases ($\phi_{12}+\phi_{34}$) is equal to 0 or π, the real part is monitored. A sum equal to $\pi/2$ gives the imaginary part.

Inspection of the relations for the response functions (20) shows that upon substitution of the time $t_1=t_{12}=0$ and $t_{34}=t_3=0$, the response functions collapse to $\exp\{-g(t_{12})\}$ for the virtual echo (R_{I} and R_{IV}) and $\exp\{-g^*(t_{12})\}$ for the conventional echo (R_{II} and R_{III}). Given the condition that the correlation function has a slow initial behaviour, it immediately follows that the response function is real at first instance (Eqs. (23)). This is reflected in the absence of any signal for the delay $t_{34}=0$ and the delay $t_{23}=0$ in Fig. 5c and d, where the imaginary part of the signal is depicted.

If one assumes that there is no energy relaxation from the system to the bath ($\lambda = 0$) as, for instance, in a stochastic model [29,45,46], there would be no signals in Fig. 5b and c. The presence of these signals directly reflects the fact that an energy relaxation process must be present in the coupled solute–solvent complex. Note that the signals measured under the cross-phase conditions (the imaginary part of the response function is probed) lead to smaller — up to tenfold — amplitudes of signals.

By the proper combination of the HSPE signals with different phase settings (Eq. (27)), the dynamic Stokes shift can be retrieved (Fig. 4, the right-hand vertical axis). Not surprisingly, for our model system an instantaneous frequency dependence that is similar to the input correlation function is found. The model system studied here illustrates the observations one is to expect in any 'real' experiment. Interferences between the different contributions should manifest themselves, both constructive and destructively, depending on the setting of the phases of the incident laser pulses.

4. Experimental

In this section we will briefly address the key features of the HSPE experiments that are performed with femtosecond excitation pulses on an IR-dye molecule in the liquid phase. The ultrashort femtosecond laser pulses used in the phase-locked experiment are generated by a cavity-dumped Ti:Sapphire laser [81]. After traversing a four-prism sequence for the dispersion control, the pulses with a duration of ~ 13 fs are directed to the phase-locked spectrometer [19]. Phase-stable laser pulse pairs are generated in two actively stabilized Mach-Zehnder interferometers. Spectral-domain interference as depicted in Fig. 3 is used to set and actively control the relative delay and phase settings of the phase-locked pulses [16–18]. Specific details on the applied phase-locking methods are discussed elsewhere [82]. The first interferometer prepares the first and second excitation pulses while the second interferometer provides the last excitation pulse in the excitation pulse sequence as well as the local oscillator field in the heterodyne detection scheme (Fig. 1). Furthermore, one of the pulse pairs is delayed with respect to the other with a delay stage.

After traversing the interferometers and the appropriate delay stages, the phase-locked pulse pairs are directed towards a reflective folding section in which they are focused in a thin (~ 100 μm) sample jet (Fig. 6). By flowing the sample in a high speed jet though the foci of the laser beams, effects of multiple interactions (such as long-term accumulated photo-decomposition and thermal accumulation effects) are prevented. After the sample a photodiode is used to detect the HSPE signal. The signals from the pre-amplified silicon photodiodes are fed into a series of lock-in amplifiers referenced to the sum frequency of the mechanical double slot chopper. The mechanical chopper is placed in such a way that one ring of slots chops the beam carrying the first pulse whereas the second slotted ring chops the beam carrying the second pulse.

Given the applied double-modulation scheme, the detected signal comprises three contributions which arise from the different sequential interactions with the third and fourth pulses: E_1–E_2–E_3–E_4, E_1–E_2–E_3–E_3 and E_1–E_2–E_4–E_4. Only the first term depends on all four pulses and is the signal of interest. The latter two terms are phase-locked pump–probe signals (PLPP) [83] which can be acquired separately by either blocking beam 4 (E_1–E_2–E_3–E_3) or beam 3 (E_1–E_2–E_4–E_4). The resulting HSPE signal is given by the total measured response minus the two separately measured PLPP baseline contributions.

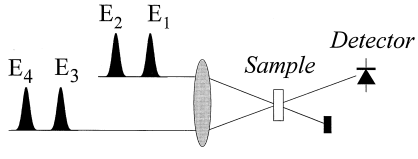

Fig. 6. Layout of the HSPE experiment. Two phase-locked pulse pairs ($E_1 - E_2$) and ($E_3 - E_4$) are focussed in the sample. The HSPE signal emitted in the direction of the pulses E_3 and E_4, is detected by a photodiode.

As a sample, DTTCI (3,3′-diethylthiatricarbocyanine iodide, Lambda Physik) dissolved in ethylene glycol (Merck p.A.) is used, with an optical density OD $\approx$ 0.1. As was pointed out in Section 2.1, a low OD is an important prerequisite to avoid interference between the HSPE signal and free-induction decay induced by the third and fourth pulses. The energies of excitation pulses were as low as 50–100 pJ which insures negligibly small contributions from the higher than third-order polarization (Section 2.1).

5. Results and discussion

In this section we report on a series of HSPE experiment performed on the probe molecule DTTCI dissolved in ethylene glycol. The results of the measurements are presented and the dependence of the measured signals on the solvation dynamics is addressed. After a discussion of the general features of the experimental data, the results are simulated using the MBO model. Finally, we present the correlation function that characterizes the solvation dynamics of the specific solute–solvent complex studied.

5.1. HSPE signals

In the HSPE experiments different cuts through the multi-dimensional space can be taken. With respect to the settings of the phases, we will only present here the results with the relative phase settings ϕ_{12} and ϕ_{34} equal to 0 and/or $\pi/2$. As we discussed in Section 2.3, these four combinations present a full orthogonal base to which all other signals measured with any particular phase setting, can be projected.

We record the HSPE signals at different settings of t_{13} to illustrate the dependence on the solvation dynamics along the t_{13} coordinate. The delay t_{12} is set to 40 fs which, from one hand, is long enough to avoid any temporal overlap between the first and second excitation pulses. On the other hand, at $t_{12} = 40$ fs the electronic coherence has not decayed completely and therefore still yields an appreciable third-order nonlinear signal. We also explored different settings of the delay t_{12} but the relevant results are presented elsewhere [19,82]. In the experiments the delay t_{34} between the third pulse (the last in the pulse sequence that induces the nonlinear response) and the local oscillator pulse (the fourth pulse in the experiment, Fig. 1) is scanned to evaluate the temporal shape and phase of the HSPE signal. Fig. 7 displays the HSPE signals for the four settings of the relative phases within the two pulse pairs and four settings of the waiting time t_{13}.

As has been discussed before (Section 2), two contributions add up to form the final HSPE signal [19,84]. The rephasing signal results from the conventional echo signal whereas the non-rephasing diagrams lead to the virtual echo [75–77]. Contrary to the homodyne-detected stimulated photon echo, the virtual echo presents a significant contribution and can by no means be ignored in the HSPE experiment. The interference between these contributions can be either constructive or destructive. In the first case the total signal is enhanced whereas in the latter case a suppression of the signal occurs. Furthermore, for the delay time t_{34} equal to zero both the rephasing and non-rephasing contribution have equal amplitude. Destructive interference between the two contributions thus leads to a full cancellation of the signal.

Comparing the results of the HSPE experiments (Fig. 7) with the signals calculated for the model system (Fig. 5), one can see a noticeable correspondence between them. Although we have no a priori knowledge of the systems correlation function nor the system dynamics, we are already in a position to raise some interesting points based on the aforementioned similarity.

We first focus on Fig. 7a ($\phi_{12} = 0$, $\phi_{34} = 0$). The signal measured at a delay time $t_{13} = 210$ fs shows that there is no prominent delayed response. Based on this fact one can conclude that on the time scale of $t \approx 200$ fs a significant decay of the correlation function has already happened, thereby moving the maximum of the transient response towards zero delay. Furthermore, with the decrease of the correlation function in time the virtual echo becomes more and more significant, causing the resulting HSPE signal to peak at zero delay. The further decay of the correlation function is evident from the fact that the HSPE signal narrows as the delay t_{13} is changed to longer times.

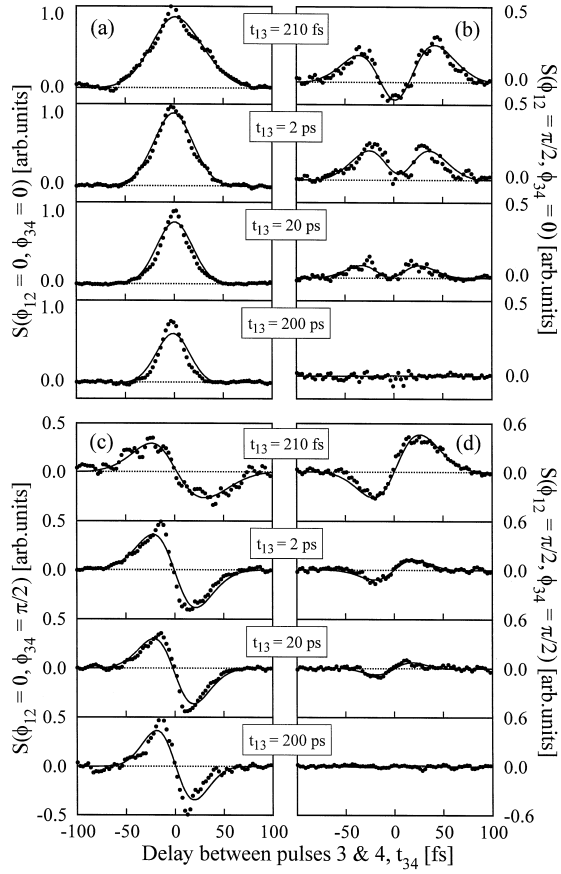

Fig. 7. Heterodyne detected stimulated photon echo signals for DTTCI in EG, measured under four orthogonal phase settings: (a) $\phi_{12} = 0$, $\phi_{34} = 0$; (b) $\phi_{12} = \pi/2$, $\phi_{34} = 0$; (c) $\phi_{12} = 0$, $\phi_{34} = \pi/2$; and (d) $\phi_{12} = \pi/2$, $\phi_{34} = \pi/2$. The settings of t_{13} are indicated in the figure. The setting of the delay t_{12} is $t_{12} = 40$ fs. The experimental data are depicted by solid circles, the fit to the data based on the MBO model is shown by the solid line.

Careful inspection of Fig. 7a ($t_{13} = 210$ fs) shows a slight signal-shape asymmetry to exist with a longer tail for positive delays. This asymmetry is caused by the action of intramolecular vibrational dynamics. In these circumstances, as pointed out before [85,86], the timing of the optical pulses in an echo experiment is of crucial importance. In fact, the delay between the first and the third interactions (t_{13}) determines whether the vibrational dynamics either enhance ($\omega_{\mathrm{vib}} t_{13} = 2\pi(n + \frac{1}{2})$) or slow down ($\omega_{\mathrm{vib}} t_{13} = 2\pi n$) the echo decay. These settings of the delay t_{13} correspond to specific positions of the vibrational wavepacket on the excited-state surface. For $t_{13} = 2\pi n/\omega_{\mathrm{vib}}$ the wavepacket has returned to its original point of excitation on the upper potential, for $t_{13} = 2\pi(n + \frac{1}{2})/\omega_{\mathrm{vib}}$ the wave packet is at its outer turning point. The steeper signal tail for negative t_{34} is a result of incomplete mode suppression. In a previous paper [85] we have discussed these effects in greater detail, showing that time-gating of HSPE at the classical echo time leads to optimal mode suppression.

When switching from an in-phase ($\phi_{34} = 0$) heterodyne detection to an in-quadrature ($\phi_{34} = \pi/2$) detection, the signals depicted in Fig. 7c are observed. Given the in-quadrature setting of the phase ϕ_{34}, asymmetric signals along the t_{34} coordinate are measured. The deviation from the perfectly symmetric shape at $t_{13} = 210$ fs, as was previously pointed out for the in-phase combination of phases, is observed for these signals (Fig. 7c) as well. A slightly longer tail on the positive side of the t_{34}-axis is in fact noticeable for all signals measured with

the four possible phase combinations at $t_{13} = 210$ fs. For long delays t_{13}, the signal (Fig. 7c) does not disappear, it only narrows as a result of the gradual motion and eventual merging of the virtual and conventional echo maxima towards zero time. For both the signals displayed in Fig. 7a and c, a significant signal is present even for delays as long as $t_{13} = 200$ ps.

In Fig. 7b and d, the results for the in-quadrature setting of the phase $\phi_{12} = \pi/2$ are displayed. Again, the correspondence between experiment and theory is quite satisfactory at a global level (Section 3). However, in contrast with Fig. 5b, no ingrowth of the signal is observed (Fig. 7b). This observation leads to the conclusion that a significant decay of the correlation function has occurred at 200 fs. As the t_{13}-delay increases, destructive interference between the real and virtual echoes manifests itself increasingly more prominent, eventually leading to complete disappearance of the signal at $t_{13} = 200$ ps. The fact that this is not due to complete decay of the individual contributions, but rather a result of Liouville-pathway interference, follows from a comparison of Fig. 7a and c.

Note that for Fig. 7b and c only the imaginary part of the response function is probed. Based on the presence of appreciable signals at a delay $t_{13} = 210$ fs, one must conclude that on this time scale the effect of solvation dynamics is already notable. In the absence of solvation dynamics ($\lambda = 0$), the HSPE signals displayed in Fig. 7b and c would vanish. The fact that these signals are present here, implies that the Bloch descriptions as well as the stochastic modulation approach are insufficient in describing the dynamics in the liquid phase.

5.2. Reconstruction of conventional and virtual response functions from HSPE signals

The full set of orthogonal HSPE signals allows for the decomposition of the experimental data into the separate rephasing and non-rephasing contributions (consult Eqs. (12) and (14)):

$$R^{\text{echo}} \propto \{S_{\text{HSPE}}(0,0) + S_{\text{HSPE}}(\pi/2,\pi/2)\} + \text{i}\{-S_{\text{HSPE}}(0,\pi/2) + S_{\text{HSPE}}(\pi/2,0)\}, \tag{36a}$$

$$R^{\text{virt.echo}} \propto \{S_{\text{HSPE}}(0,0) - S_{\text{HSPE}}(\pi/2,\pi/2)\} - \text{i}\{-S_{\text{HSPE}}(0,\pi/2) + S_{\text{HSPE}}(\pi/2,0)\}, \tag{36b}$$

where the two arguments of the S_{HSPE} denote the phase settings ϕ_{12} and ϕ_{34}. In Fig. 8 the transient amplitude and phase of the response functions R^{echo} and $R^{\text{virt.echo}}$ are depicted for the delay $t_{13} = 210$ fs. Note that as a result of the inherent degeneracy of pulses 3 and 4 (these pulses are indistinguishable in the experiment) a seemingly non-causal (i.e., non-zero for $t_{34} < 0$) signal is obtained for the virtual echo.

For short delays ($t_{13} = 210$ fs) the conventional echo response function exhibits a shift from zero. The maximum of the trace peaks near $t_{34} \approx 20$ fs. Note that if the system's memory is perfect as is the case for

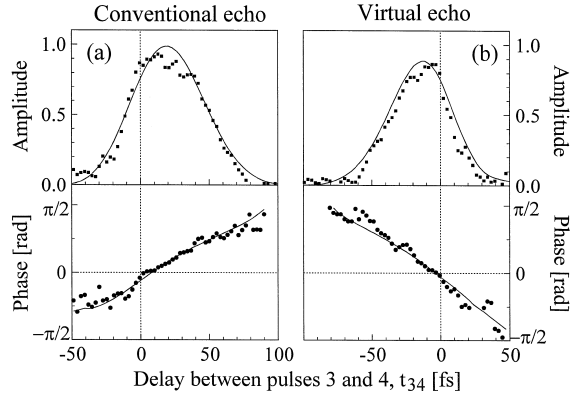

Fig. 8. Results of the reconstruction of conventional (a) and virtual (b) response functions for the data given in Fig. 7. The values of t_{12} and t_{13} are set at 40 and 210 fs, respectively. The solid lines are the results of numerical simulations with the MBO model.

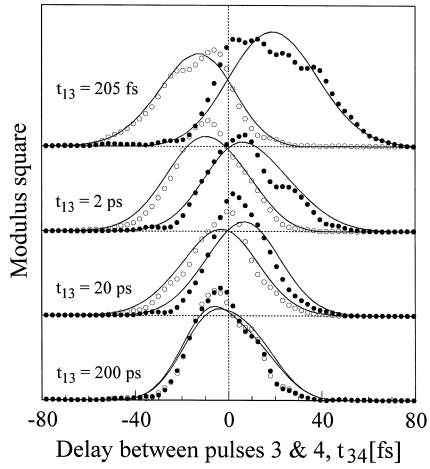

Fig. 9. Results of the construction of conventional and virtual echo signals from the data given in Fig. 7. The modulus square of the virtual (open circles) and conventional echo signal (solid circles) are given for the four settings of the delay t_{13} as listed in the figure. The solid lines are fits with the MBO model.

overwhelmingly inhomogeneous broadening, rephasing of the conventional echo should occur at $t_{34} = t_{12} = 40$ fs. The fact that this is not the case in the experiment means that on a time scale of 200 fs memory loss is already significant. However, the system has not yet been disturbed so much that it has lost its ability to exhibit some rephasing. This results in a delayed conventional echo and a small but visible tail of the virtual echo (Fig. 8).

The slight asymmetry in the amplitude of the virtual and conventional response functions is the result of the presence of vibrational modes in the probe molecule. The wavepacket dynamics associated with these modes modulate both the real part as well as the imaginary part of the response function. As a consequence, the line broadening (to a large extend related to the real part) as well as Stokes shift (primarily connected to the imaginary part) are affected. The latter effect is readily seen in the clearly different slopes of the phases of the conventional (Fig. 8a) and virtual (Fig. 8b) echoes. Inspection of the phases of both response functions shows a linear dependence of the phase on the time t_{34}. Note that for a delay $t_{34} = 0$ only the real part (zero phase) in the response function is observed, whereas for larger times t_{34} an ingrowing imaginary term is seen. A linear relation between the phase and the time t_{34} indicates a constant frequency shift in the nonlinear response function. As was mentioned in Section 3.1, this frequency shift tracks the dynamic Stokes shift as measured in fluorescence upconversion experiments (vide infra).

As the waiting time t_{13} becomes longer, the influence of the solvent fluctuations increases which results in a lower ability to exhibit rephasing. The relevant data are presented in Fig. 9. For a short delay t_{13}, the echo exhibits a delayed response. For the virtual echo trace, only a relatively small tail at the positive side of the t_{34}-axis is present. As the delay t_{13} is increased, both echoes shift towards zero and become less and less distinguishable. Eventually, for delay times $t_{13} = 200$ ps the conventional and virtual echoes merge together. The destructive interference between the two contributions thus leads to the complete disappearance of the total signal, as is observed in Fig. 7b and c.

5.3. HPSE experiments and dynamical Stokes shift

In this section we will focus on the phase of the HSPE signal as it provides a direct route to the system correlation function (Eq. (27)). Having obtained the real and imaginary parts of the third-order nonlinear

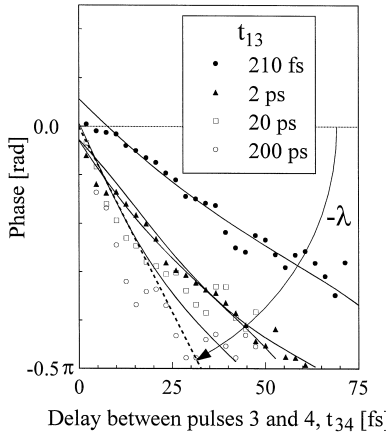

Fig. 10. Time-dependent phase of the nonlinear third-order polarization for the data given in Fig. 7. The values of waiting time t_{13} are indicated in the figure. The solid lines are results as obtained from the fit with the MBO model. The dashed line shows the maximum possible inclination determined by the steady-state Stokes shift.

polarization (by measuring the signals for different phases ϕ_{34}), we are now in a position to deduce the transient phase of the HSPE signal. In Fig. 10 we present the time-dependent phase of the HSPE signal for different waiting times t_{13}. For all t_{13} settings a nearly linear time dependence of the phase on the delay t_{34} is obtained which corresponds to constant instantaneous frequency of the emitted polarization. For the applied phase-locking technique a slope of zero means that the emitted polarization is completely in-phase with the selected lock wavelength. With the increase in the delay t_{13} a clockwise rotation of the slope of the curves is seen (Fig. 10) which is related to the dynamical Stokes shift as observed in fluorescence upconversion experiments [87–90].

In contrast with the fluorescence upconversion experiment [87–90], the HSPE measurement is sensitive to the dynamics on both the ground- and the excited-state potentials. In the former experiment, which is solely sensitive to the dynamics of the excited state, the measured shift amounts to twice the solvent reorganization energy λ. In the HSPE experiment the effective frequency shift in the signal is half the Stokes shift and thus equals the solvent reorganization energy λ (see Section 3.1). For the molecule DTTCI under study, the Stokes shift as measured in the steady-state fluorescence spectrum is $2\lambda = 470$ cm^{-1} [43]. The corresponding solvent reorganization energy of 235 cm^{-1} imposes the limiting value of the red frequency shift, indicated by an arrow in Fig. 10. Now, with Eq. (17) we can calculate the instantaneous frequency of the signal for any waiting time. For the delay $t_{13} = 210$ fs the experimentally measured shift is ~ 82 cm^{-1}, whereas for longer delays ($t_{13} = 200$ ps) the shift approaches ~ 230 cm^{-1}.

5.4. Numerical simulation of HSPE experiments

In order to model and quantify the experimental results of the HSPE experiments all data were simulated using the MBO model [68]. The crucial ingredient of the MBO model is formed by the correlation function $M(t)$. For this, we employ the results obtained from the time-resolved and time-integrated echo experiments [43]. The resulting correlation function, presented in Fig. 11, encompasses multiple dynamical aspects of the system (solute-vibrational properties) as well as the system–bath dynamics (solute–solvent interactions). For the numerical calculations of the HPSE signals the complete expressions including the finite pulse duration effects as given by Eqs. (3)–(5) were used. Other Feynman diagrams which can be omitted in case of impulse excitations, must be taken in consideration. These diagrams are attributed to the 'wrong' pulse sequences (e.g., pulses 2–1–3 and so on). The calculation algorithms were implemented in a C-program and were run on a

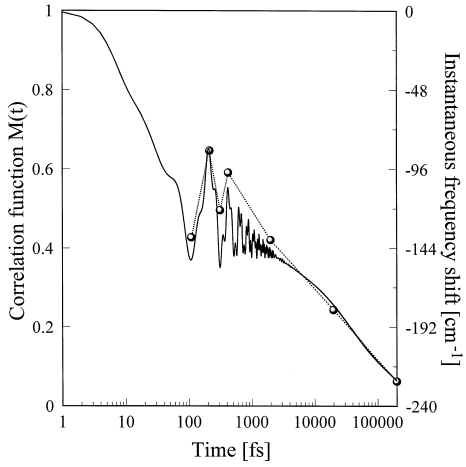

Fig. 11. The correlation function $M(t)$ used in the numerical simulations. The points mark the position of the instantaneous frequency shift (right-hand axis) as obtained from the data presented in Fig. 10. Note that the time axis is logarithmic.

32-parallel vector-processor CRAY-J932 supercomputer. As a result of the parallel processing, typical calculation times were reduced to only a couple of hours. A more detailed description on the fitting procedure can be found elsewhere [43,82].

The results of the fits to the HSPE experiments are shown in Figs. 7–10 by solid lines. Slight deviations in the phases (with a maximum of ± 10 degrees) were allowed to account for the experimental uncertainty in absolute phase settings. The locking-wavelength was chosen according the experimental values and was not a fitting parameter. The laser carrier wavelength was set to 797 ± 2 nm for different experiments.

Let us first discuss the fits to the HSPE data presented in Fig. 7. As can be inferred from the various fits, there is an excellent correspondence between the experimental HSPE results and the numerical simulations. Based on these findings one can conclude that the correlation function as obtained via the time-resolved data [43], directly predicts most of the HSPE results. The significance of this finding lays in the fact that time-resolved studies are not extremely sensitive to the imaginary part of the nonlinear response functions while the HSPE experiments are [43]. However, within the MBO model there is a direct relation between the line broadening effect (real part of $g(t)$) and the frequency-shift effect (imaginary part of $g(t)$) as dictated by the fluctuation-dissipation theorem [68]. Therefore, one can conclude that the use of the MBO model is quite appropriate to the description of solvation dynamics.

The conventional and virtual echoes can be also reconstructed in numerical simulations. The fitted data processed in the same way as the experimental results are depicted in Fig. 8. Given the good fit to the original HSPE data, it is not surprising that the reconstructed signals exhibit the same close resemblance to the measured data. The same holds for the longer time-scale data as depicted in Fig. 9.

Fig. 10 displays the time dependence of the phase of the induced nonlinear polarization. As the delay t_{13} increases, a gradual decrease of the instantaneous frequency of the emitted polarization is observed. From a linear fit to the time dependence of the phase (Fig. 10), the value of the instantaneous frequency (relative to the locking frequency) can be derived. These data superimposed on the original correlation function are depicted in Fig. 11. Apparently, the measurements of the instantaneous frequency closely tracks the correlation function. The HSPE technique is thus a direct probe of the time-dependent frequency of the emitted nonlinear polarization. In the MBO model the instantaneous frequency directly projects onto the system–bath correlation function. HSPE thus yields direct access to solvent reorganization dynamics on a femtosecond time scale.

6. Conclusions

In this paper, we have presented a theoretical description of heterodyne detected photon echo, a technique that allows measurement of the phase and amplitude of the nonlinear optical polarization. Detailed knowledge of the induced nonlinear polarization is important for testing the applicability of different models to describe the system of interest. For example, the Bloch [44] and stochastic modulation models [45,46] predict that there is only an in-phase component of the induced polarization. In the multimode Brownian oscillator model the appearance of an imaginary, in-quadrature component of the polarization can be explained as a result of energy dissipation of the optically excited system interacting with a bath. From this viewpoint it is essential to measure both the real and imaginary parts independently to check whether the system under study complies with the restrictions set by a dynamical model.

The HSPE experiment is a multi-dimensional (three times, two phases and signal amplitude) experiment. As a result of this multi-dimensionality, a full exploration of the complete space is virtually impossible. In order to extract the most valuable information, certain cuts through the 6-D surface have to be carefully selected. Several examples of these kinds of projection experiments are phase-locked pump–probe [83], mode-suppression [85,86], and Liouville-space pathways interference [84].

HSPE experiments were successfully exploited for the study of solvation dynamics on the infrared dye molecule DTTCI. Based on the measured data, the real and imaginary terms of the induced polarization were retrieved on a femtosecond time scale. Especially the waiting time (t_{13}) dependence of the signal phase provides a valuable connection to the instantaneous frequency of the emitted polarization, which directly reflects the correlation function. Using HSPE solvent reorganization and energy relaxation from the solute to the bath can be probed in real time. In this sense HSPE is a useful alternative to fluorescence upconversion, applicable also in the case of a small Stokes shift.

In order to simulate the nonlinear optical signal transients, the multimode Brownian oscillator (MBO) model was used. This model provides an excellent description of the measured transients with as input the correlation function derived from time-gated echo experiments [43]. We emphasize that both the intramolecular as well as the solute–solvent dynamics are reflected in the results. We note that the results presented in this paper were obtained at room temperature. A full temperature-dependent study is required to explore the need of introducing non-Markovian oscillators [31,91] or anharmonic coupling effects [92–98].

Similar time-gated echo experiments by heterodyne detection of the transient signal with an external local oscillator have been performed on semiconductors by Bigot et al. [99]. These experiments were performed on a 100 fs time scale, without active control over the phases of either the excitation or the local oscillator pulses. With the ability to phase-lock the excitation pulses as well as the local oscillator, the amplitude and phase of the transient signal can now be directly and accurately time-resolved. Furthermore, an active and stable control over the phases of the exciting laser pulses is a necessary requirement to observe interference effects between different Liouville-space pathways. The possibility to distinguish between the different Liouville-space pathways allows the separation of the so-called conventional echo and virtual echo contributions to the total HSPE signal.

Next to HSPE several other photon echo methods can been applied to unravel the system–bath dynamics. Among these methods, the echo-peak shift (EPS) provides a direct probe of the correlation function, except at early times [43]. Further insight into the dynamics governing the initial part of the correlation function can be obtained by employing more advanced — yet more eleborate — detection methods. One example is the time-gated experiment, where the echo signal is mixed with a gate pulse in a nonlinear optical crystal and the transient amplitude of the echo signal is time-resolved [41–43]. This way, both the fast as well as the slow time-scale components in the correlation function can be detailed [43].

All of the above methods employ homodyne-detection, which implies that information on the phase of the induced polarization is lost. The latter information, however, is crucial, if one wants to resolve the time dependence of the mean energy, as reflected in the dynamical Stokes shift. To measure the phase of the induced

polarization, a heterodyne-detected photon echo (HSPE) experiment, as presented in this paper should be performed. Here the in-phase (real) and in-quadrature (imaginary) components of the nonlinear polarization and the nonlinear response functions can be probed. Furthermore, from HSPE one can deduce the instantaneous frequency of the echo signal, that tracks the dynamical Stokes shift.

The characterization of weak nonlinear optical signals is currently a hot issue. Quite recently, a breakthrough was made in the development of techniques and algorithms for the complete characterization of the optical pulses [100–105]. However, since the methods are based on a nonlinear interaction of the unknown pulse with some instantaneously responding material, a relative strong laser field is required. Of course, this situation is rarely found for signal levels in nonlinear optical experiments. The latter restriction is released when TADPOLE [103–105] is used where spectral interference between a local oscillator and a weak optical field is used to reconstruct the unknown transient signal. This promising spectral-domain interference technique has recently been applied to the investigation of dynamics in semiconductors [106] and liquids [107].

Acknowledgements

We are grateful to F. de Haan for providing us with software for efficient data collection and handling. The investigations were supported by the Netherlands Foundation for Chemical Research (SON) and Physical Research (FOM) with financial aid from the Netherlands Organization for the Advancement of Science (NWO).

References

[1] U. Keller (Ed.), Ultrashort Pulse Generation (special issue), Appl. Phys. B 65 (1997).
[2] A. Baltuška, Z. Wei, M.S. Pshenichnikov, D.A. Wiersma, Opt. Lett. 22 (1997) 102.
[3] M. Nisoli, S. De Silvestri, O. Svelto, Appl. Phys. Lett. 68 (1996) 2793.
[4] R. Sciposz, K. Ferencz, Ch. Spielmann, F. Krausz, Opt. Lett. 19 (1994) 201.
[5] R. Sciposz, A. Kohazi-Kis, Proc. SPIE 2253 (1994) 140.
[6] G.R. Fleming, Chemical Applications of Ultrafast Spectroscopy, Oxford University Press, Oxford, 1986.
[7] D.A. Wiersma (Ed.), Femtosecond Reaction Dynamics, North Holland, Amsterdam, 1994.
[8] A.H. Zewail (Ed.), Femtochemistry: Ultrafast Dynamics of the Chemical Bond, World Scientific, Singapore, 1994.
[9] Picosecond Phenomena, Springer Series in Chemical Physics, Springer, Berlin, Issues I(1978), II(1980), III(1982), IV(1984).
[10] Ultrafast Phenomena, Springer Series in Chemical Physics, Springer, Berlin, Issues V(1986), VI(1988), VII(1990), VIII(1992), IX(1994), X(1996).
[11] J.T. Hynes, Annu. Rev. Phys. Chem. 36 (1985) 573.
[12] G.R. Fleming, P.G. Wolynes, Phys. Today 43 (1990) 36.
[13] J.D. Simon, Acc. Chem. Res. 21 (1988) 128.
[14] P.F. Barbara, W. Jarzeba, Adv. Photochem. 15 (1990) 1.
[15] P.J. Rossky, J.D. Simon, Nature (London) 370 (1994) 263.
[16] N.F. Scherer, A.J. Ruggiero, M. Du, G.R. Fleming, J. Chem. Phys. 93 (1990) 856.
[17] N.F. Scherer, R.J. Carlson, A. Matro, M. Du, A.J. Ruggiero, V. Romero-Rochin, J.A. Cina, G.R. Fleming, S.A. Rice, Chem. Phys. 95 (1991) 1487.
[18] N.F. Scherer, A. Matro, L.D. Ziegler, M. Du, R.J. Carlson, J.A. Cina, G.R. Fleming, J. Chem. Phys. 96 (1992) 4180.
[19] W.P. de Boeij, M.S. Pshenichnikov, D.A. Wiersma, Chem. Phys. Lett. 238 (1995) 1.
[20] M. Cho, N.F. Scherer, G.R. Fleming, S. Mukamel, J. Chem. Phys. 96 (1992) 5618.
[21] P.C. Becker, H.L. Fragnito, J.-Y. Bigot, C.H. Brito Cruz, R.L. Fork, C.V. Shank, Phys. Rev. Lett. 63 (1989) 505.
[22] W.T. Pollard, H.L. Fragnito, J.-Y. Bigot, C.V. Shank, R.A. Mathies, Chem. Phys. Lett. 168 (239) (1990) 239.
[23] J.-Y. Bigot, M.T. Portella, R.W. Schoenlein, C.J. Bardeen, A. Migus, C.V. Shank, Phys. Rev. Lett. 66 (1991) 1138.
[24] E.T.J. Nibbering, D.A. Wiersma, K. Duppen, Phys. Rev. Lett. 66 (1991) 2464.
[25] E.T.J. Nibbering, D.A. Wiersma, K. Duppen, J. Photochem. Photobiol. A 62 (1992) 347.
[26] R. Zhang, T.-S. Yang, A.B. Myers, Chem. Phys. Lett. 112 (1993) 541.
[27] K. Duppen, F. de Haan, E.T.J. Nibbering, D.A. Wiersma, Phys. Rev. A 47 (1993) 5120.
[28] T. Joo, A.C. Albrecht, Chem. Phys. 176 (1993) 233.

[29] E.T.J. Nibbering, D.A. Wiersma, K. Duppen, Chem. Phys. 183 (1994) 167.
[30] K. Duppen, E.T.J. Nibbering, D.A. Wiersma, in: D.A. Wiersma (Ed.), Femtosecond Reaction Dynamics, North Holland, Amsterdam, 1994, pp. 197–208.
[31] W.P. de Boeij, M.S. Pshenichnikov, K. Duppen, D.A. Wiersma, Chem. Phys. Lett. 224 (1994) 243.
[32] C.J. Bardeen, C.V. Shank, Chem. Phys. Lett. 226 (1994) 310.
[33] S.J. Rosenthal, B.J. Schwartz, P.J. Rossky, Chem. Phys. Lett. 229 (1994) 443.
[34] M. Cho, G.R. Fleming, J. Chem. Phys. 98 (1994) 3478.
[35] T. Joo, Y. Jia, G.R. Fleming, J. Phys. Chem. 102 (1995) 4063.
[36] T. Joo, Y. Jia, J.-Y. Yu, M.J. Lang, G.R. Fleming, J. Chem. Phys. 104 (1996) 6089.
[37] M. Cho, J.-Y. Yu, T. Joo, Y. Nagasawa, S.A. Pasino, G.R. Fleming, J. Phys. Chem. 100 (1996) 11944.
[38] G.R. Fleming, M. Cho, Annu. Rev. Phys. Chem. 47 (1996) 109.
[39] P. Vöhringer, D.C. Arnett, R.A. Westervelt, M.J. Feldstein, N.F. Scherer, J. Chem. Phys. 102 (1995) 4027.
[40] T.-S. Yang, P. Vöhringer, D.C. Arnett, N.F. Scherer, J. Chem. Phys. 103 (1995) 8346.
[41] M.S. Pshenichnikov, K. Duppen, D.A. Wiersma, Phys. Rev. Lett. 74 (1995) 674.
[42] P. Vöhringer, D.C. Arnett, T.-S. Yang, N.F. Scherer, Chem. Phys. Lett. 237 (1995) 387.
[43] W.P. de Boeij, M.S. Pshenichnikov, D.A. Wiersma, J. Phys. Chem. 100 (1996) 11806.
[44] F. Bloch, Phys. Rev. 70 (1946) 460.
[45] J.R. Klauder, P.W. Anderson, Phys. Rev. 125 (1962) 912.
[46] R. Kubo, Adv. Chem. Phys. 15 (1969) 101.
[47] Y.J. Yan, M. Sparpaglione, S. Mukamel, J. Phys. Chem. 92 (1988) 4842.
[48] S. Mukamel, Y.J. Yan, Acc. Chem. Res. 22 (1989) 310.
[49] J.N.L. Connor, N. Sutin, A.H. Zewail (Eds.), R.A. Marcus (special issue), J. Phys. Chem. 90 (1986).
[50] M. Sparpaglione, S. Mukamel, J. Chem. Phys. 88 (1988) 3263.
[51] M. Sparpaglione, S. Mukamel, J. Chem. Phys. 88 (1988) 4300.
[52] Y. Jia, D.M. Jonas, T. Joo, Y. Nagasawa, M.J. Lang, G.R. Fleming, J. Phys. Chem. 99 (1995) 6263.
[53] T. Joo, Y. Jia, J.-Y. Yu, D.M. Jonas, G.R. Fleming, J. Phys. Chem. 100 (1996) 2399.
[54] R. Jimenez, S.N. Dikshit, S.E. Bradforth, G.R. Fleming, J. Phys. Chem. 100 (1996) 6825.
[55] D.M. Jonas, M.L. Lang, Y. Nagasawa, T. Joo, G.R. Fleming, J. Phys. Chem. 100 (1996) 12660.
[56] M. Aihara, Phys. Rev. B 25 (1982) 53.
[57] Y.J. Yan, S. Mukamel, J. Chem. Phys. 89 (1988) 5160.
[58] Y.J. Yan, S. Mukamel, Phys. Rev. A 41 (1990) 6485.
[59] Y.J. Yan, S. Mukamel, J. Chem. Phys. 94 (1991) 179.
[60] S. Mukamel, Adv. Phys. Chem. 70 (I) (1998) 165.
[61] S. Mukamel, Annu. Rev. Phys. Chem. 41 (1990) 647.
[62] A.O. Caldiera, A.J. Leggett, Physics A 121 (1983) 587.
[63] H. Grabert, P. Schramm, G.L. Ingold, Phys. Rep. 168 (1988) 115.
[64] M. Cho, N.F. Scherer, G.R. Fleming, S. Mukamel, J. Chem. Phys. 96 (1992) 5618.
[65] L.E. Fried, N. Bernstein, S. Mukamel, Phys. Rev. Lett. 68 (1992) 1842.
[66] Y. Tanimura, S. Mukamel, Phys. Rev. E 47 (1993) 118.
[67] Y. Gu, A. Widom, P.M. Champion, J. Chem. Phys. 100 (1994) 2547.
[68] S. Mukamel, Principles of Nonlinear Optical Spectroscopy, Oxford University Press, New York, 1995.
[69] L. Allen, J.H. Eberly, Optical Resonance and Two-level Atoms, Wiley-Interscience, New York, 1975.
[70] P.N. Butcher, D. Cotter, The elements of non-linear optics, in: P.L. Knight, W.J. Firth (Eds.), Cambridge Studies in Modern Optics, vol. 9, Cambridge University Press, Cambridge, 1995.
[71] Y.R. Shen, The Principles of Nonlinear Optics, Wiley, New York, 1984.
[72] T. Brabec, F. Krausz, Phys. Rev. Lett. 78 (1997) 3282.
[73] M. Chachisvilis, H. Fidder, V. Sundström, Chem. Phys. Lett 234 (1995) 141.
[74] A. Kummrow, M.F. Emde, M.S. Pshenichnikov, D.A. Wiersma, J. Phys. Chem. (submitted).
[75] A.L. Bloom, Phys. Rev. 98 (1955) 1105.
[76] R.L. Schoemaker, Coherent transient infrared spectroscopy, in: J.I. Steinfeld (Ed.), Laser and Coherence Spectroscopy, Plenum, New York, 1978, p.294.
[77] K. Duppen, D.A. Wiersma, J. Opt. Soc. Am. B 3 (1986) 614.
[78] D.H. Reitze, A.M. Weiner, D.E. Leaird, Appl. Phys. Lett. 61 (1992) 1260.
[79] A. Efimov, C. Schaffer, D.H. Reitze, J. Opt. Soc. Am. B 12 (1995) 1968.
[80] D. Yelin, D. Meshulach, Y. Silberberg, Opt. Lett. 22 (1997) 1793.
[81] M.S. Pshenichnikov, W.P. de Boeij, D.A. Wiersma, Opt. Lett. 19 (1994) 572.
[82] W.P. de Boeij, Ph.D. Thesis, University of Groningen, Groningen, 1997.

[83] W.P. de Boeij, M.S. Pshenichnikov, D.A. Wiersma, Chem. Phys. Lett. 247 (1995) 264.
[84] M.S. Pshenichnikov, W.P. de Boeij, D.A. Wiersma, Phys. Rev. Lett. 76 (1996) 4701.
[85] W.P. de Boeij, M.S. Pshenichnikov, D.A. Wiersma, J. Chem. Phys. 105 (1996) 2953.
[86] W.P. de Boeij, M.S. Pshenichnikov, D.A. Wiersma, Ultrafast phenomena, X, in: P.F. Barbara, J.G. Fujimoto, W.H. Knox, W. Zinth (Eds.), Springer Series in Chemical Physics, vol. 62, Springer, Berlin, 1996, pp. 223–224.
[87] R. Jimenez, G.R. Fleming, P.V. Kumar, M. Maroncelli, Nature (London) 369 (1994) 471.
[88] S.J. Rosenthal, R. Jimenez, G.R. Fleming, P.V. Kumar, M. Maroncelli, J. Mol. Liq. 60 (1994) 25.
[89] M.L. Horng, J. Gardecki, A. Papazyan, M. Maroncelli, J. Phys. Chem. 99 (1995) 17311.
[90] T. Gustavsson, G. Baldacchino, J.-C. Mialocq, S. Pommeret, Chem. Phys. Lett. 236 (1995) 587.
[91] N.P. Ernsting, N. Eilers-König, K. Kemeter, S. Kovalenko, J. Ruthmann, Fast elementary processes in chemical and biological systems, in: A. Tramer (Ed.), AIP Conference Proceedings, vol. 364, Woodbury, New York, 1995, p.441.
[92] T. Reinot, W.-H. Kim, J.M. Hayes, G.J. Small, J. Chem. Phys. 104 (1996) 793.
[93] T. Reinot, J.M. Hayes, G.J. Small, J. Chem. Phys. 106 (1997) 457.
[94] M. Aihara, Phys. Rev. B 25 (1982) 53.
[95] A.J. Taylor, D.J. Erskine, C.L. Tang, Chem. Phys. Lett. 103 (1984) 430.
[96] S.F. Fischer, A. Laubereau, Chem. Phys. Lett. 35 (1975) 6.
[97] D.J. Diestler, A.H. Zewail, J. Chem. Phys. 71 (1979) 3103.
[98] Y. Tanimura, K. Okumura, J. Chem. Phys. 106 (1997) 2078.
[99] J.-Y. Bigot, M.-A. Mycek, S. Weiss, R.G. Ulbrich, D.S. Chemla, Phys. Rev. Lett. 70 (1993) 3307.
[100] D.J. Kane, R. Trebino, J. Quant. Electr. 29 (1993) 571.
[101] K.W. DeLong, R. Trebino, J. Opt. Soc. Am. B 11 (1994) 1595.
[102] D.N. Fittinghoff, K.W. DeLong, R. Trebino, C.L. Ladera, J. Opt. Soc. Am. B 12 (1995) 1955.
[103] D.N. Fittinghoff, J.L. Bowie, J.N. Sweetser, R.T. Jennings, M.A. Krümbugel, K.W. DeLong, R. Trebino, I.A. Walmsley, Opt. Lett. 21 (1996) 884.
[104] D.N. Fittinghoff, J.L. Bowie, J.N. Sweetser, R.T. Jennings, M.A. Krümbugel, K.W. DeLong, R. Trebino, I.A. Walmsley, Opt. Lett. 21 (1996) 1313, erratum.
[105] W.J. Walecki, D.N. Fittinghoff, A.L. Smirl, R. Trebino, C.L. Ladera, Opt. Lett. 22 (1997) 81.
[106] J.P. Likforman, M. Joffre, R. Panel, Opt. Lett. 22 (1997) 1104.
[107] M.F. Emde, W.P. de Boeij, M.S. Pshenichnikov, D.A. Wiersma, Opt. Lett. 22 (1997) 1338.